

CHEMISTRY

Addressed realization of multication complex arrangements in metal-organic frameworks

Celia Castillo-Blas,¹ Víctor A. de la Peña-O'Shea,² Inés Puente-Orench,^{3,4} Julio Romero de Paz,⁵ Regino Sáez-Puche,⁶ Enrique Gutiérrez-Puebla,¹ Felipe Gándara,^{1*} Ángeles Monge^{1*}

The preparation of materials with structures composed of multiple metal cations that occupy specific sites is challenging owing to the difficulty of simultaneously addressing the incorporation of different elements at desired precise positions. We report how it is possible to use a metal-organic framework (MOF) built with a rod-shaped inorganic secondary building unit (SBU) to combine multiple metal elements at specific positions in a manner that is controllable at atomic and mesoscopic scales. Through the combination of four different metal elements at judiciously selected molar ratios, 20 MOFs of different compositions and the same topology have been prepared and characterized. The use of diffraction techniques, supported by density functional theory calculations, has led us to determine various possible atomic arrangements of the metal cations within the SBUs. In addition, seven of the compounds combine multiple types of atomic arrangements, which are mesoscopically distributed along the crystals. Given the large diversity and importance of rod-based MOFs, we believe that these findings offer a new general strategy to produce complex materials with required compositions and controllable arrangements of the metal cations for desired applications.

INTRODUCTION

Materials with structures comprising the presence of multiple metal elements are important in many fields because the combination of different metal cations typically offers new or enhanced properties that are not attainable with the use of just one metal. Thus, mixed-metal oxides and salts are extensively used as anode materials in batteries (1); superconductivity has been demonstrated in several families of multimetal materials, such as oxides or pnictides, whose structures are made of the combination of several cations (2–5). Doped metal oxides are frequently used in optical devices, and diluted magnets are prepared by the introduction of a paramagnetic element, such as cobalt, into the structure of zinc or titanium oxide, with these materials exhibiting magnetoresistance properties (4, 6–8). Mixed-metal oxides are also good catalysts in key chemical transformations (9). However, it still remains a challenge to synthesize new materials with structures where the disposition of the metal elements is highly controllable. Up to now, control over the arrangement of the different elements in most of the existing materials has been limited or inexistent. Limitations regarding the amount and nature of the elements that can be combined within a same structure also exist. Metal-organic frameworks (MOFs) are a class of crystalline materials, composed by the combination of metal clusters [secondary building units (SBUs)] and organic linkers (10). Although MOFs have been traditionally constructed with just one metal cation, they have recently shown the potential to incorporate multiple metal elements within the same crystal structure by either a postsynthetic transmetalation process (11) or the combination of multiple metal salts during the MOF synthesis (12), in some cases resulting in the formation

of cation domains (13). However, thus far, most of the reported systems lack fundamental control on the disposition of the used metal elements, neither at the atomic, nano-, or mesoscopic scale.

Here, we report a platform MOF that allows the directed incorporation of multiple metal elements into the same structure at precise locations, resulting in materials where the arrangement of the metal cations is controllable at various length scales through the use of an appropriate SBU and framework topology. The judicious selection of a molar code defined by the initial molar ratio of the used metal elements drives the incorporation and arrangement of the MOF metal components (i) at the atomic and nanoscales, by producing sequences of elements within the same SBU, and (ii) at the mesoscopic scale, by producing crystals where SBUs of different compositions are preferentially located at different shells of the crystals.

Synthesis of MOFs with multiple metal cations from an adaptable SBU

Our strategy to prepare new multimetal systems of addressable complexity involves the selection of a MOF whose crystallization process has been proven to be kinetically driven. A MOF structure whose formation is thermodynamically highly favorable for a given cation will not allow the corresponding solid-solution systems to be obtained, whereas a MOF structure whose formation is kinetically governed may be in an equilibrium that will allow the incorporation of additional elements into the framework during the synthesis reaction (14). This is the case of ZnPF-1, a MOF built with 4,4'-(hexafluoroisopropylidene) bis(benzoic acid) (H₂hfipbb) as organic linker. This MOF has a helical, rod-shaped inorganic SBU formed by tetrahedral zinc atoms and a three-dimensional structure with square and hexagonal channels running parallel to the *c* axis (Fig. 1). It crystallizes in the hexagonal *P*6₄22 space group [*a* = 21.22(1) Å and *c* = 7.710(5) Å] (15). Despite the extensive use of this organic linker to prepare different MOFs with various metal elements, thus far this MOF topology has only been reported with the use of zinc. By maintaining a constant metal-to-linker molar ratio of 1.65 (section S1 and table S1), the addition of cobalt nitrate in the initial mixture results in the formation of needle-like crystals with intense blue color. We coined the term “molar code” to indicate the

¹Departamento de Nuevas Arquitecturas en Química de Materiales, Materials Science Factory, Instituto de Ciencia de Materiales de Madrid–Consejo Superior de Investigaciones Científicas, Sor Juana Inés de la Cruz 3, Madrid 28049, Spain. ²IMDEA Energy Institute, Móstoles Technology Park, Avenida Ramón de la Sagra 3, 28935 Móstoles, Madrid, Spain. ³Instituto de Ciencia de Materiales de Aragón, Pedro Cerbuna 12, 50009 Zaragoza, Spain. ⁴Institut Laue Langevin, 71 Avenue des Martyrs, 38042 Grenoble, France. ⁵Centros de Apoyo a la Investigación Técnicas Físicas, Facultad de Ciencias Físicas, Universidad Complutense de Madrid, Avenida Complutense s/n, 28040 Madrid, Spain. ⁶Departamento de Química Inorgánica, Facultad de Ciencias Químicas, Universidad Complutense de Madrid, 28040 Madrid, Spain.

*Corresponding author. Email: gandara@icmm.csic.es (F.G.); amonge@icmm.csic.es (Á.M.)

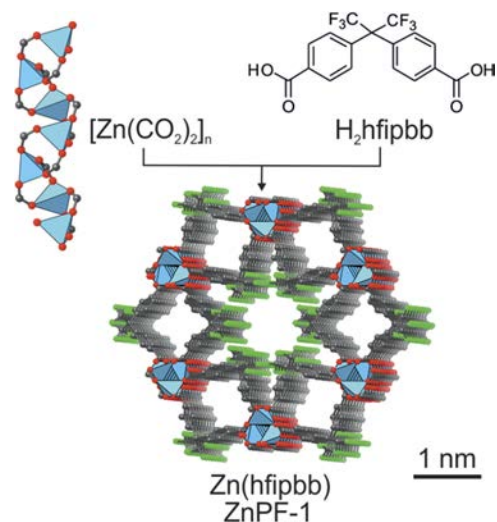


Fig. 1. ZnPF-1 is formed by the combination of H₂hfipbb with a helical inorganic SBU where the zinc atoms are tetrahedrally coordinated. O, C, and F atoms are depicted as red, gray, and green balls, respectively, and pale blue tetrahedra represent zinc cations.

selected molar relationship between metal elements. Thus, Zn:Co molar codes of 1:1, 1:2, 1:4, and 1:10 were selected to prepare the corresponding MOFs of variable composition (Scheme 1). The chemical composition of the bulk samples was determined by means of inductively coupled plasma (ICP) and elemental analysis (table S2). A room temperature x-ray diffraction (XRD) study of a single crystal prepared from a Zn:Co 1:2 molar code proved that the sample was isostructural to the original ZnPF-1, with the crystallographic metal position occupied by both zinc and cobalt (section S2).

Through scanning electron microscopy (SEM) and energy-dispersive x-ray spectroscopy (EDS) analyses of MOFs, it was consistently found that the amount of cobalt is larger in the external areas of the crystals (Fig. 2 and section S3). In addition, the crystals were found to be hollow, with a central hole running along the longest crystal axis. This hollow morphology and the concentration gradient are consistent with an Ostwald ripening process (16), where zinc-rich crystals are initially formed, followed by partial redissolution of the inner parts and crystal growing of the external faces through the incorporation of cobalt in larger proportion. A synthesis and kinetic study carried out for the MOF prepared from a Zn:Co 1:2 molar code further validated this point, as evidenced by the increase in cobalt incorporation with longer heating times up to 20 hours (section S4).

A cobalt-rich sample was produced by introducing a sufficiently large amount of cobalt in the molar code. Thus, the sample prepared from a Zn:Co 1:10 molar code has a chemical formula of Zn_{0.21}Co_{0.79}(hfipbb). Unexpectedly, the x-ray single-crystal study shows a unit cell with a doubled *c* parameter and *P*6₃22 space group. This lattice constant change arises from the splitting of the crystallographic metal sites within the SBUs, which are now composed of alternating tetrahedral and octahedral metal sites (Fig. 3, bottom). The results of the XRD refinement suggest that the octahedral sites are occupied by cobalt atoms, whereas the tetrahedral ones are occupied by both zinc and cobalt. Despite the change in the coordination environment, the transformed SBU remains unaltered in its points of extension, which, in turn, define the MOF topology (17).

To obtain further insight into this phase transformation, we performed a low-temperature single-crystal diffraction study for the sam-

ple prepared from a Zn:Co 1:2 molar code. As described above, the room temperature data showed the presence of just one tetrahedral metal site, with mixed Zn/Co occupancy. We then collected XRD data at 200, 150, 100, and 50 K. No changes were observed for the 200 K data, as compared to room temperature. A phase transition was first observed at 150 K, with the corresponding doubling of the *c* lattice parameter. Consequently, two crystallographic metal positions are present in the SBU, with a distorted tetrahedral coordination environment, denoted as Td1 and Td2 in Fig. 3. Analysis of the difference Fourier maps showed a large residual electron density near the metal atoms, which we assign as additional metal sites with partial occupancy (Td1b and Td2b), arising from the ongoing atomic rearrangement. However, the presence of residual electron density indicates that the transformation is not complete yet. This is only achieved at 50 K, where the crystal structure is equivalent to the one determined for the Zn:Co 1:10 sample, with both an octahedral and a tetrahedral site. The results of this study suggest that the presence of cobalt in the structure has a stabilizing effect on the octahedral site. On the contrary, ZnPF-1 does not undergo any phase transformation, because no change in the unit cell was observed for a crystal collected at 50 K. Because zinc and cobalt have similar atomic numbers, it is not possible to unambiguously determine the occupancy of the metal sites with just XRD. We therefore performed a neutron diffraction experiment for this purpose.


Unveiling atomic arrangement

To uncover the atomic arrangement of the metal cations within the solid-solution MOF crystals, we completed a neutron powder diffraction (NPD) study at variable temperatures for zinc- and cobalt-rich samples. In particular, we selected MOFs prepared from Zn:Co 1:2 and Zn:Co 1:10 molar codes. NPD is a particularly suitable technique because of the different scattering length of these elements, in contrast to XRD.

Thermodiffraction experiments evidenced a structural phase transition at 140 and 80 K for the Zn:Co 1:2 and Zn:Co 1:10 samples, respectively (section S5). The Rietveld refinement for the room temperature NPD pattern of the Zn/Co 1:2 sample indicates the sole presence of the original phase with only one tetrahedral metal site in the SBU, which was refined as being occupied by Co or Zn, with ratio coincident with the one determined by ICP analysis (Fig. 4A). For the low-temperature pattern (50 K), a satisfactory refinement could not be achieved by considering just the transformed crystal cell. A careful analysis shows the presence of a remaining amount of untransformed crystal phase. The presence of ZnPF-1 crystals has been ruled out because the SEM and EDS analyses prove the presence of cobalt in all crystals. We can therefore conclude that both phases are coexisting within the MOF crystals, as a result of the compositional variations.

A multiphase Rietveld refinement was carried out, and the percentage of each phase was estimated on the basis of the ratio of the integrated intensities. The best refinement results were obtained for a combination of the original and transformed phases at ratios of 15 and 85%, respectively (Fig. 4B). The metal sites in the original phase (exclusively tetrahedral) were refined as zinc atoms, whereas for the transformed phase, the tetrahedral site was refined as fully occupied by zinc, and the octahedral site as fully occupied by cobalt. These results, along with the presence of holes and compositional gradient in the crystals, indicate that this MOF is composed of an inner core with SBUs made of zinc atoms and an outer shell with SBUs made of alternating zinc and cobalt atoms. At room temperature, both atoms are in a tetrahedral environment, whereas by lowering the temperature, only the cobalt atoms become octahedral, resulting in the unit cell change.

Molar code				MOF formula	Atomic arrangement	Mesoscopic arrangement
Zn	Mn	Co	Ca			
1	0	1	0	$Zn_{0.89}Co_{0.11}(hfiipbb)$	Core Shell	Multisequence arrangement
1	0	2	0	$Zn_{0.59}Co_{0.41}(hfiipbb)$	Core Shell	
1	0	4	0	$Zn_{0.55}Co_{0.45}(hfiipbb)$	Core Shell	
1	0	10	0	$Zn_{0.21}Co_{0.79}(hfiipbb)$	Core Medium shell Shell	
1	0	1	1	$Zn_{0.72}Co_{0.17}Ca_{0.11}(hfiipbb)$	Core Shell	
1	0	4	4	$Zn_{0.33}Co_{0.37}Ca_{0.30}(hfiipbb)$	Core Shell	
1	0	1	8	$Zn_{0.37}Co_{0.14}Ca_{0.49}(hfiipbb)$	Core Shell	
1	1	0	0	$Zn_{0.50}Mn_{0.50}(hfiipbb)$		Single-sequence arrangement
1	0	0	1	$Zn_{0.96}Ca_{0.04}(hfiipbb)$		
1	0	0	2	$Zn_{0.94}Ca_{0.06}(hfiipbb)$		
1	0	0	4	$Zn_{0.64}Ca_{0.36}(hfiipbb)$		
1	0	0	10	$Zn_{0.48}Ca_{0.52}(hfiipbb)$		
1	1	1	0	$Zn_{0.44}Mn_{0.44}Co_{0.12}(hfiipbb)^*$		
2	1	1	0	$Zn_{0.54}Mn_{0.37}Co_{0.09}(hfiipbb)$		
1	2	1	0	$Zn_{0.37}Mn_{0.50}Co_{0.13}(hfiipbb)$		
1	1	2	0	$Zn_{0.32}Mn_{0.39}Co_{0.28}(hfiipbb)^*$		
1	1	8	0	$Zn_{0.22}Mn_{0.32}Co_{0.46}(hfiipbb)^*$		
1	3	9	0	$Zn_{0.12}Mn_{0.42}Co_{0.46}(hfiipbb)^*$		
1	1	0	1	$Zn_{0.48}Mn_{0.42}Ca_{0.10}(hfiipbb)$		
1	1	0	8	$Zn_{0.52}Mn_{0.30}Ca_{0.18}(hfiipbb)^*$		



 ▲ Tetrahedral Zn ◆ Octahedral Mn ▲ Tetrahedral Co ◆ Octahedral Co ◆ Octahedral Ca

* This MOF has different possible sequences of SBUs

Scheme 1. Selection of appropriate molar codes express the formation of different kinds of atomically sequenced inorganic SBUs. Corresponding MOF crystals might include multiple SBUs mesoscopically arranged, or just one.

In the case of the sample prepared from a Zn:Co 1:10 molar code, the room temperature NPD pattern indicates the presence of both phases. These two unit cells at room temperature could not be detected by single-crystal x-ray analysis because of the overlapping of reflection positions (the hkl reflections in the original phase appear at virtually the same position of the corresponding $hkl/2$ reflections of the transformed

phase). Through a multiphase Rietveld refinement, the percentage of both phases at room temperature was estimated to be 67 and 33% for the original and transformed one, respectively (Fig. 4C). The portion of the crystal corresponding to the transformed phase was refined to be composed exclusively of cobalt, having both tetrahedral and octahedral environments. The portion of the crystal corresponding to the

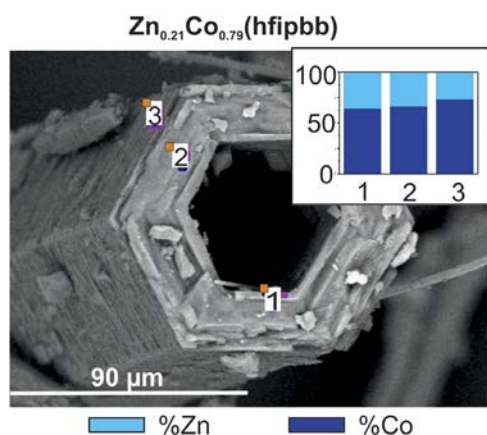


Fig. 2. SEM image and EDS analysis of $Zn_{0.21}Co_{0.79}(hfipbb)$. Metal atomic percent was determined with the spectra recorded at the various points of the crystal indicated in the image.

original phase was refined to be composed of both zinc (30%) and cobalt (70%) (Fig. 4D). By lowering the temperature (10 K), most of this portion of the crystal is also transformed. However, the 10 K NPD pattern shows the presence of small shoulders in the (102) and (212) diffraction peaks, which indicate that there is also a residual portion of the crystal that retains the original phase [the shoulders corresponding to the (101) and (211) reflections of the untransformed phase]. Consequently, this MOF has three compositional domains: a small core (no more than 5% according to NPD Rietveld refinement) exclusively made of zinc, followed by a shell where the SBUs are composed of zinc and cobalt cations at a Zn/Co 3:7 ratio, all of them being tetrahedral at room temperature, whereas at low temperature, part of the cobalt cations become octahedral. In the third outer shell (around 33%), the SBUs are exclusively composed of cobalt cations with alternating tetrahedral and octahedral coordination environments.

Expanding the use of molar codes to produce MOFs with controllable metal arrangements

The selected inorganic SBU has shown adaptability and dynamism through the possibility of including multiple elements with variable coordination environments, such as cobalt, while maintaining the overall MOF topology and connectivity, which is seemingly directed by the use of zinc. By selecting the appropriate molar code, it is possible to control the introduced amount of a second element, as well as its arrangement and coordination environment. On the other hand, if an element with clear propensity for an octahedral coordination environment is chosen, then this should preferentially occupy certain sites in the inorganic SBUs. A MOF with a $Zn_{0.5}Mn_{0.5}(hfipbb)$ composition was prepared by starting from a Zn:Mn 1:1 molar code. The single-crystal XRD study shows lattice parameters of $a = 21.2897(5)$ Å and $c = 15.1282(5)$ Å and $P6_522$ space group, with the SBUs being formed by alternating tetrahedral zinc and octahedral manganese atoms. Crystals of this MOF are not hollow, and the EDS study shows that there are no compositional gradients along the crystals (Fig. 5A). NPD Rietveld refinement proves that there is only one type of unit cell present at room temperature (Fig. 5B).

Moreover, the introduction of manganese into the molar code allows for the homogeneous distribution of cobalt. Thus, in contrast to the Zn/Co systems, ternary MOFs with molar codes including Zn/Mn/Co, do not exhibit compositional gradients, and all three elements are equally distributed in all areas of the crystals, as shown by the EDS analysis.

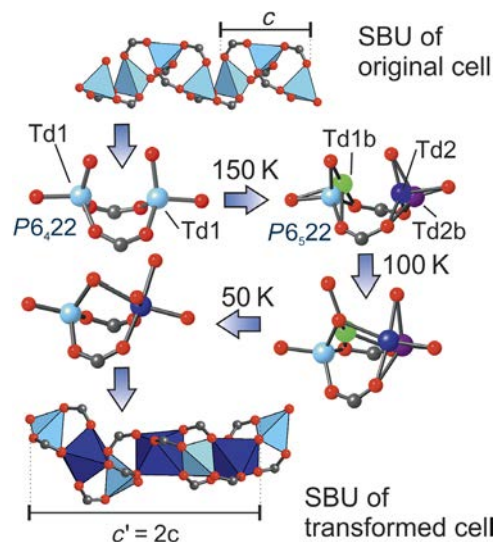


Fig. 3. The inorganic SBU might adapt to include octahedrally coordinated cations, which results in a unit cell transformation where the c parameter is doubled. This transformation was monitored by temperature-variable single-crystal XRD and NPD. O, C, and F atoms are depicted as red, gray, and green balls, respectively. Pale blue tetrahedra and dark blue octahedra might represent different metal elements (see text). For the phase transformation depiction, the color of the balls representing the metal elements corresponds to independent crystallographic sites.

The room temperature single-crystal XRD studies demonstrate that these MOFs have unit cells with double c parameter and the presence of both octahedral and tetrahedral metal sites in the SBUs. Because zinc and manganese exclusively occupy the tetrahedral or octahedral sites, respectively, by adjusting the molar codes, it is possible to address the incorporation of cobalt at either tetrahedral, octahedral, or both sites, as deduced by the chemical composition of the resulting MOFs. For example, a MOF obtained from a Zn:Mn:Co 1:2:1 molar code has a formula $Zn_{0.37}Mn_{0.5}Co_{0.13}(hfipbb)$, which implies that one of five tetrahedral sites in the SBUs is occupied by cobalt, resulting in an atomic sequence, as shown in Scheme 1. Correspondingly, a MOF obtained from a Zn:Mn:Co 2:1:1 molar code and formula $Zn_{0.54}Mn_{0.37}Co_{0.09}(hfipbb)$ expresses an SBU with an atomic sequence, as depicted in Scheme 1, where one of five octahedral sites is occupied by cobalt. In both cases, other possible combinations involving the coexistence of several compositional domains are ruled out by the compositional homogeneity demonstrated by the EDS analysis. Single-crystal XRD analyses further support the location of the cobalt atoms at the proposed sites.

On the other hand, for MOFs prepared from molar codes that contain the same zinc and manganese number, cobalt is directed to be occupying both the octahedral and tetrahedral sites. In samples prepared from Zn:Mn:Co 1:1:1, 1:1:2, and 1:1:8 molar codes and formulae $Zn_{0.44}Mn_{0.44}Co_{0.12}(hfipbb)$, $Zn_{0.32}Mn_{0.39}Co_{0.28}(hfipbb)$, and $Zn_{0.22}Mn_{0.32}Co_{0.46}(hfipbb)$, the cobalt atoms are inevitably occupying both tetrahedral and octahedral sites. In these cases, as shown in the scheme, there are several possible atomic sequences that fulfill the coordination environment requirement for zinc and manganese and agree with the determined composition (Fig. 6A). In all cases, neutron powder thermodiffraction experiments indicate that only one crystalline phase with double c parameter is formed (section S5).

Definition of appropriate molar codes allows different degrees of compositional and structural complexities, which are addressable by

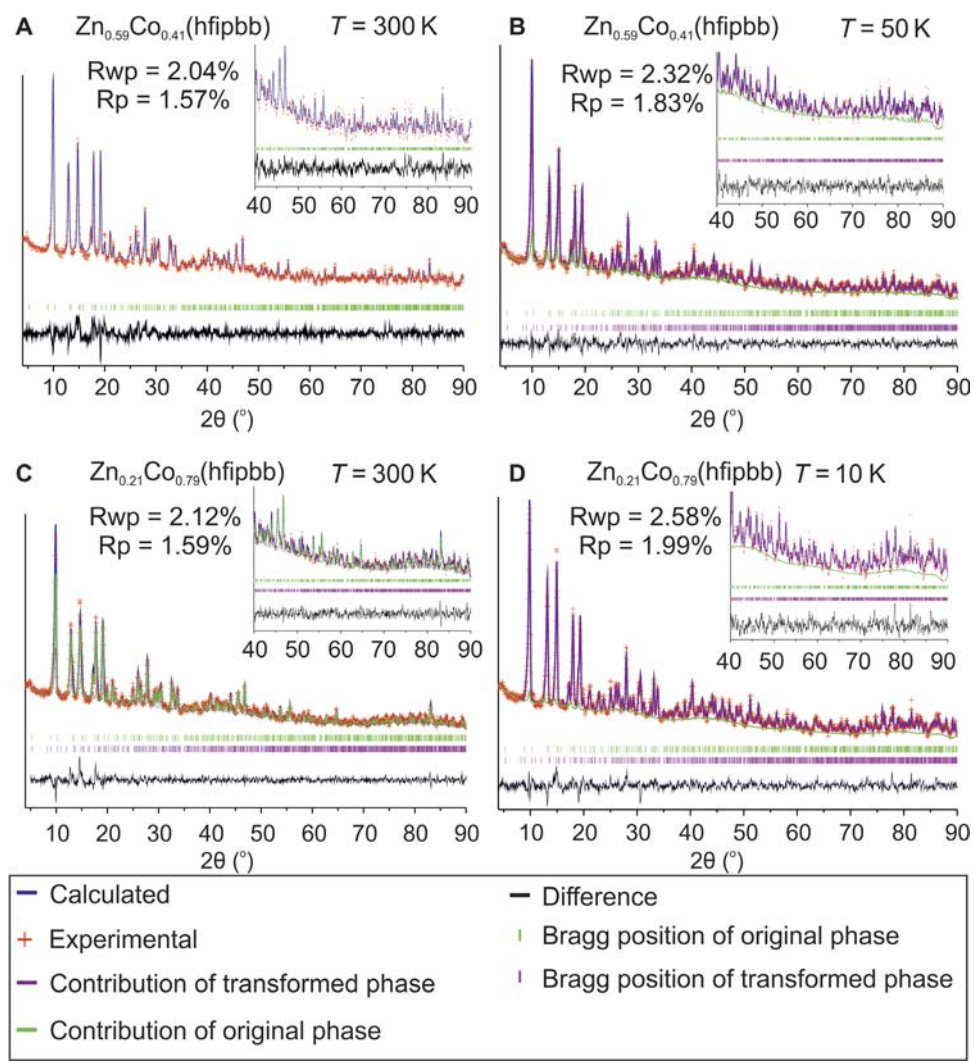


Fig. 4. NDP Rietveld refinements. In the case of the $\text{Zn}_{0.59}\text{Co}_{0.41}(\text{hfipbb})$ MOF, the refinements indicate the presence of only the original cell at 300 K (A) and both original (15%) and transformed (85%) cells at 50 K (B). In the case of the $\text{Zn}_{0.21}\text{Co}_{0.79}(\text{hfipbb})$ MOF, both original (66%) and transformed (33%) unit cells are present at 300 K (C), whereas the transformation is almost complete (95%) at 10 K (D). In all cases, the composition of the metal sites was refined. For the multiphase refinements (B to D), the percentage of each unit cell was determined by the ratio of the integrated intensities. Rp and Rwp are unweighted and weighted agreement profile factors, respectively.

the selected combination of elements, each one of them with a particular role. Thus, zinc is the structure-directing element which is necessary to obtain the desired MOF SBU and topology. On the other hand, MOFs prepared from molar codes including manganese, demonstrate a homogeneous compositional arrangement, providing atomic control on the SBU sequences. Finally, mesoscopic compositional arrangements might appear through the use of cobalt.

This complexity control is achievable even with the incorporation of other metal elements. Thus, it is also possible to include nontransition metal elements in the molar codes to incorporate them in MOFs with desired complexity.

As proof of concept, we have included calcium into a MOF structure that is not obtainable with the use of only this element. We have prepared MOFs from Zn:Ca 1:1 and 1:2 molar codes. These MOFs only contain small amounts of calcium in the structure, their formulae being $\text{Zn}_{0.96}\text{Ca}_{0.04}(\text{hfipbb})$ and $\text{Zn}_{0.94}\text{Ca}_{0.06}(\text{hfipbb})$, and homogeneous distribution of calcium along the crystals. Larger amounts of calcium can be incorporated by using molar codes with larger calcium numbers.

Thus, the use of a Zn:Ca 1:4 molar code results in a MOF with the formula $\text{Zn}_{0.64}\text{Ca}_{0.36}(\text{hfipbb})$. Room temperature single-crystal XRD shows lattice parameters $a = 21.2239(8)$ Å and $c = 15.5784(6)$ Å and $P6_122$ space groups, with two metal sites in the SBUs. One is exclusively occupied by tetrahedral zinc atoms, and the other one is occupied by calcium (72%) or zinc (28%). In this second site, the metal coordination environment is octahedral when occupied by calcium and tetrahedral when occupied by zinc. Thus, the SBUs comprise alternating zinc and calcium atoms, with 28% of calcium being substituted by zinc. No compositional gradients are observed in the EDS analysis (Fig. 6B), which indicates a regular distribution of zinc domains within a zinc-calcium SBU.

The pure zinc-calcium SBU can be expressed by using a Zn:Ca 1:10 molar code. The corresponding MOF has $\text{Zn}_{0.48}\text{Ca}_{0.52}(\text{hfipbb})$ formula, and EDS indicates compositional homogeneity.

Molar codes combining zinc, calcium, and manganese express SBUs with additional atomic sequences, as proposed in Scheme 1. Zn:Mn:Ca 1:1:1 and 1:1:8 molar codes result in MOFs with $\text{Zn}_{0.48}\text{Mn}_{0.42}\text{Ca}_{0.10}(\text{hfipbb})$

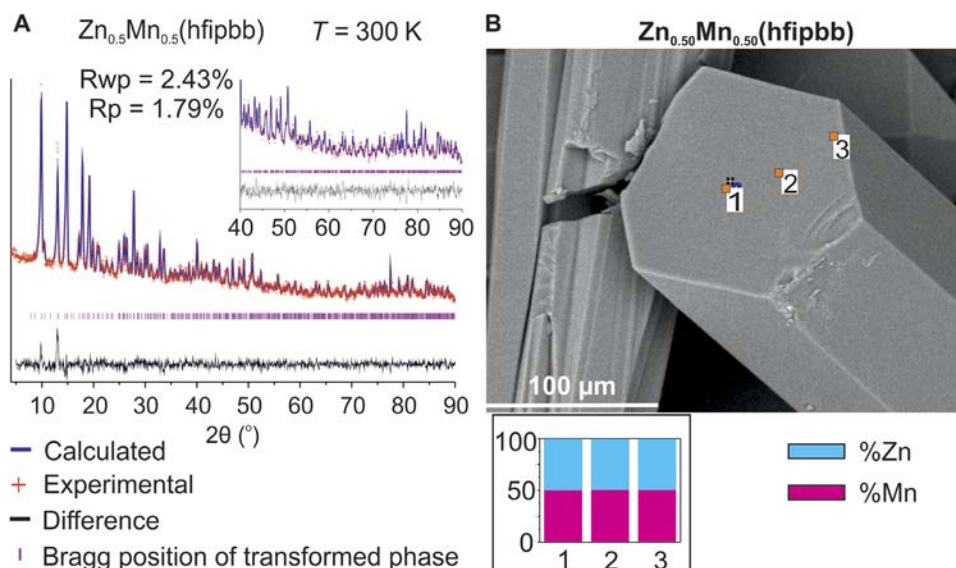


Fig. 5. NPD and EDS analysis of $\text{Zn}_{0.50}\text{Mn}_{0.50}(\text{hfipbb})$ MOF. (A) For the $\text{Zn}_{0.50}\text{Mn}_{0.50}(\text{hfipbb})$ MOF, the Rietveld refinement is consistent with presence of only a cell with alternating tetrahedral zinc–octahedral manganese SBUs at 300 K. (B) SEM and EDS analyses show homogeneous distribution of metal elements in $\text{Zn}_{0.50}\text{Mn}_{0.50}(\text{hfipbb})$.

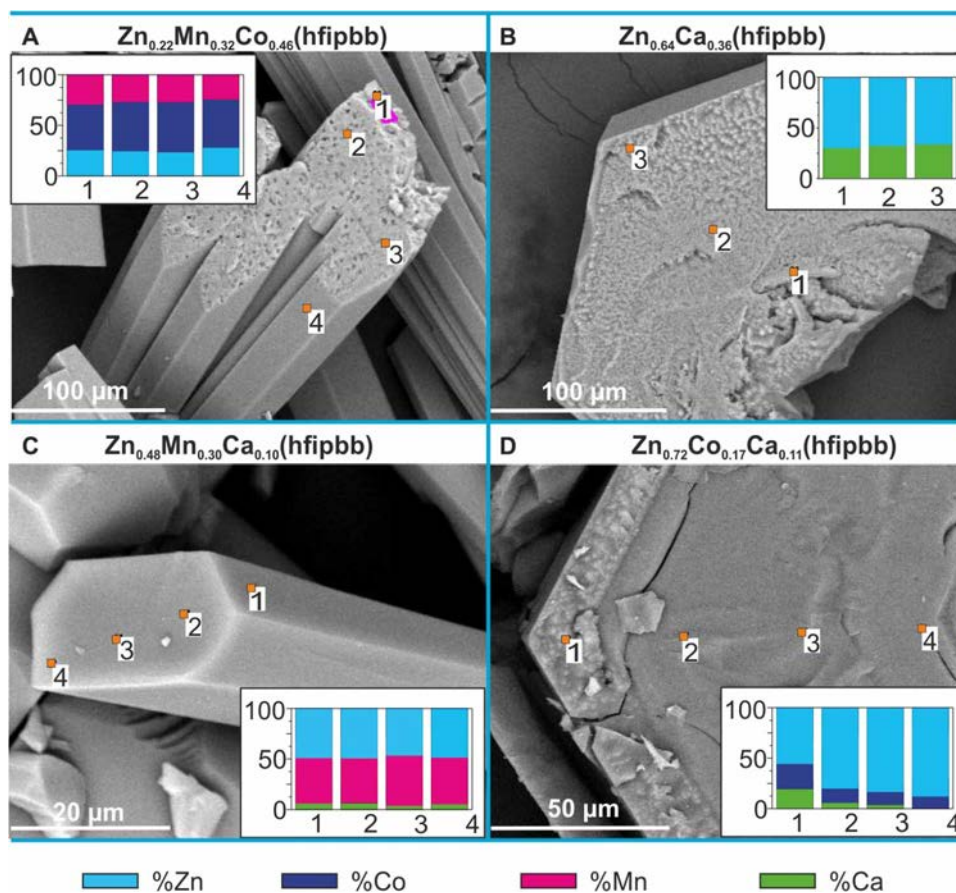


Fig. 6. SEM images and EDS analysis of selected MOFs. Representative examples of different MOFs prepared from various molar codes are shown in (A) to (D), demonstrating both homogeneous arrangements (A to C) and compositional gradients (D). Metal atomic percent was determined with the spectra recorded at multiple points or areas of each crystal, as indicated in the images.

and $\text{Zn}_{0.52}\text{Mn}_{0.30}\text{Ca}_{0.18}$ (hfipbb) formulae, respectively. Single-crystal XRD experiments show SBUs with tetrahedral zinc atoms, and octahedral calcium and manganese atoms, which are occupying the same crystallographic site. EDS demonstrates homogeneous distribution (Fig. 6C).

Mesoscopic control in the incorporation of calcium at preferential crystal faces is possible by combining it with cobalt. Thus, the MOF prepared from a Zn:Co:Ca 1:1:1 molar code displays a clear compositional gradient, where calcium is preferentially located at the external faces, according to the EDS analysis (Fig. 6D). The SEM images show crystals with well-differentiated core and external shells. The core is mainly composed of zinc and a small amount of cobalt (ca. 10%, as determined by EDS), whereas the external shell contains all three elements. Finally, the use of Zn:Co:Ca 1:4:4 and 1:1:8 molar codes result in MOFs with the formulae $\text{Zn}_{0.33}\text{Co}_{0.37}\text{Ca}_{0.30}$ (hfipbb) and $\text{Zn}_{0.37}\text{Co}_{0.14}\text{Ca}_{0.49}$ (hfipbb). These MOFs show mesoscopic compositional gradients of zinc and cobalt, whereas the amount of calcium is homogeneously distributed, according to EDS analysis. Single-crystal XRD experiments show that, as expected, calcium is occupying the octahedral sites, whereas cobalt might be at both tetrahedral and octahedral ones.

Formation energies (ΔE_{Form}) determined by ab initio density functional theory (DFT) calculations corroborate the importance of the kinetic control on the first stages of the synthesis (section S6). Crystal models of MOFs consisting of SBUs formed by alternating tetrahedral zinc atoms and octahedral zinc, cobalt, manganese, or calcium atoms, and another model with alternating tetrahedral and octahedral cobalt atoms were geometrically optimized, in all cases converging to stable structures with the same topology, although no symmetry constraints were imposed. The hypothetical phase consisting of tetrahedral and octahedral zinc atoms was the only one with a higher formation energy than the original ZnPF-1 phase, which is consistent with the impossibility of transformation of the MOF made of only zinc. On the other hand, the calculations also corroborate that the concentration gradient is consistent with an Ostwald ripening process, because the use of cobalt, calcium, and manganese leads to a decrease in the formation energy. The pure cobalt phase is the most energetically stable, which is also consistent with the formation of this phase in the outer shells of samples made with longer synthesis time. In addition, density of states reveals that the geometry distortion produced by the introduction of a second cation stabilizes the orbitals with higher occupation while destabilizing those with lower occupation, thus breaking the degeneracy of the octahedral geometry.

Compositional and structural complexities define physical properties of MOFs

The results of this work offer a new platform to obtain complex structures where the arrangement of the metal cations can be virtually controlled on demand. Considering that the properties of materials are dictated by their composition and precise atomic and mesoscopic structures, we believe that our findings will be relevant to various fields. The case of the magnetic properties of MOFs is illustrated; magnetic properties are determined by the combination of these factors, namely, the geometry of the SBUs, the atomic distribution of cations, and the possible mesoscopic interaction among SBUs. Thus, in the case of the MOF prepared from a Zn:Co 1:2 molar code, ferromagnetism is developed within the SBUs below 15 K, and interchain antiferromagnetic interactions acquire a long-range character below 7 K, although a large-enough applied magnetic field produces a metamagnetic transition, giving rise to a long-range ferromagnetic state. In the MOF prepared

from a Zn:Co 1:10 molar code, where the larger incorporation of cobalt in the SBU forces the presence of cobalt neighbor polyhedra, canted antiferromagnetism is developed within the SBUs in such a way that a rather small net magnetization appears below 35.8 K within the SBU composed exclusively of cobalt, and an additional contribution at lower temperatures comes from the SBU with 30% of the tetrahedral sites occupied by cobalt, where the number of consecutive cobalt cations is smaller (section S7). The ability to produce MOFs with controllable metal arrangements shown in this work opens the possibility to stimulate or block a specific superexchange pathway to develop a specific magnetic interaction within SBUs.

In view of the large number of existing MOFs that are constructed from many diverse rod-shaped SBUs (18), it might be anticipated that this method will be generalized to prepare new materials with topologies and structures fit for specific applications where multiple metal cations can be arranged at desired atomic positions, as well as mesoscopically distributed. During the revision of this work, Kim and Coskun (19) reported the preparation of bimetallic MOF-74 through a heterogeneous phase synthetic method, where the resulting materials have nearly 1:1 metal ratios regardless of the initially used ratios.

MATERIALS AND METHODS

Synthetic procedure

All reagents and solvents used were commercially available and used as received without further purification: H_2hfipbb (98%; ABCR GmbH and Co.); zinc nitrate, $\text{Zn}(\text{NO}_3)_2 \cdot 6\text{H}_2\text{O}$ ($\geq 99\%$; Scharlab); calcium nitrate, $\text{Ca}(\text{NO}_3)_2 \cdot 4\text{H}_2\text{O}$ ($\geq 99\%$; Sigma-Aldrich); manganese chloride, $\text{MnCl}_2 \cdot 4\text{H}_2\text{O}$ ($\geq 98\%$; Sigma-Aldrich); and cobalt nitrate, $\text{Co}(\text{NO}_3)_2 \cdot 6\text{H}_2\text{O}$ ($\geq 99\%$; Sigma-Aldrich). General synthetic procedure for all the MOFs involved the dissolution of the selected metal salts and the organic linker in a water/ethanol/nitric acid solvent mixture, followed by heating at 170°C for an overnight period. An illustrative example of the synthesis procedure is given here for the $\text{Zn}_{0.59}\text{Co}_{0.41}$ (hfipbb) compound: H_2hfipbb (78 mg, 0.2 mmol), $\text{Zn}(\text{NO}_3)_2 \cdot 6\text{H}_2\text{O}$ (33 mg, 0.11 mmol), and $\text{Co}(\text{NO}_3)_2 \cdot 6\text{H}_2\text{O}$ (66 mg, 0.22 mmol) were dissolved in 5 ml of distilled water, 5 ml of absolute ethanol, and 300 μl of a 1 M HNO_3 solution. The mixture was stirred at room temperature for 5 min, placed in a Teflon-lined steel autoclave, and heated at 170°C overnight. After cooling to room temperature, blue needle-shaped crystals were filtered off, washed with water and acetone, and dried under vacuum (61 mg of solid recovered). The rest of the materials were similarly prepared using the amounts of metal salt specified in table S1 and keeping the same amounts of linker and solvents.

Single-crystal XRD

Crystals were selected using a polarized optical microscope for a single-crystal XRD experiment. Single-crystal x-ray data were collected in Bruker four-circle kappa diffractometers equipped with a Cu INCOATED microsource, operated at 30-W power (45 kV, 0.60 mA) to generate Cu $K\alpha$ radiation ($\lambda = 1.54178 \text{ \AA}$), and a Bruker VANTEC-500 area detector (microgap technology) or a Bruker PHOTON II area detector (CPAD Technology). Diffraction data were collected, exploring over the reciprocal space in a combination of ϕ and ω scans to reach a resolution of 0.85 \AA , with a completeness $>95\%$ and a redundancy >3 . For this, either a generic hemisphere collection strategy or a specific one determined using Bruker APEX3 (20) software suite was used. The exposure time was adjusted on the basis of size and diffracting quality of the

specimens, each exposure covering 1° in ω or ϕ . Unit cell dimensions were determined for least-squares fit of reflections with $I > 4\sigma$. The structures were solved by direct methods implemented in the SHELX package. The hydrogen atoms were fixed at their calculated positions using distances and angle constraints. All calculations were performed using APEX3 software for data collection and OLEX2-1.2 (21) and SHELXTL (22) to resolve and refine the structure. All nonhydrogen atoms were anisotropically refined.

Powder XRD

Powder XRD (PXRD) patterns were measured using a Bruker D8 diffractometer with a copper source operated at 1600 W, with step size = 0.02° and exposure time = 0.5 s per step. PXRD measurements were used to check the purity of the obtained microcrystalline products by a comparison of the experimental results with the calculated patterns obtained from single-crystal XRD data.

SEM and EDS analyses

SEM images and EDS were collected using an S-3000N microscope, equipped with an ESED and an INCAx-sight from Oxford Instruments, respectively. All samples were prepared for SEM and EDS analyses by dispersing the material onto a double-sided adhesive conductive carbon tape that was attached to a flat aluminum sample holder and were metalized using a 12-nm gold layer with a Quorum Q150T-S sputter.

Neutron powder diffraction

NPD experiments were performed on the high-resolution multidetector and on the high-intensity powder diffractometers D2B and D1B, respectively, at the Institut Laue-Langevin in Grenoble (France). The samples were contained in a 6-mm cylindrical vanadium can and placed on a cryostat (vanadium-tailed 69ILHV25 and Orange Cryostat for D1B and D2B, respectively). The data sets were collected with calibrated neutrons of wavelengths 2.5260 and 1.5923 Å for D1B and D2B, respectively. Neutron thermodiffractograms were collected using the high-flux D1B diffractometer, between 10 and 300 K, with a heating rate of 0.5 K/min, covering a 2θ range of 0.2° to 128° . The high-resolution neutron diffraction profiles were collected at 300 K for $\text{Zn}_{0.59}\text{Co}_{0.41}$ (hfiipbb), $\text{Zn}_{0.21}\text{Co}_{0.79}$ (hfiipbb), and $\text{Zn}_{0.50}\text{Mn}_{0.50}$ (hfiipbb); at 50 K for $\text{Zn}_{0.59}\text{Co}_{0.41}$ (hfiipbb); and at 10 K for $\text{Zn}_{0.21}\text{Co}_{0.79}$ (hfiipbb) in the D2B diffractometer, covering a 2θ range of 0.2° to 150° , every 0.05° . The data reduction (including the application of some basic operations as those related with the addition of several patterns or detector efficiency corrections) was carried out with the LAMP software. Rietveld refinements were performed using the Reflex module of Materials Studio 8.0 (23). Initial atomic coordinates were taken from the single crystal-determined structures.

DFT calculations

Theoretical calculations by periodic DFT were carried out using the geometry obtained in single-crystal resolution. The density functional plane-wave calculations were carried out by means of the VASP package (24, 25), considering spin polarization and dipole corrections explicitly. The total energies corresponding to the optimized geometries of all samples were calculated using the spin-polarized version of the exchange and correlation functional of Perdew and Wang (26, 27). The effect of the core electrons on the valence electron density was described by the projector augmented wave method (28, 29). The cutoff for the kinetic energy of the plane waves was set to 415 eV to ensure a total energy convergence better than 10^{-6} eV/K.

Magnetic susceptibility measurements

Magnetization measurements were carried out on polycrystalline samples using a superconducting quantum interference device magnetometer (Quantum Design, model MPMS-XL). The temperature dependence of the molar magnetic susceptibility (χ) was obtained from the dc magnetization (M) measured with an applied magnetic field (H) during warming of the sample from 2 up to 300 K. Zero-field cooling and field-cooling measurement modes were used. In the former, the sample was cooled down from room temperature to 2 K in zero field, and in the latter, the sample was cooled down in the measuring H . The magnetic field dependence of the dc magnetization $M(H)$ was obtained at different temperatures up to ± 5 T. The temperature dependence of the real and imaginary parts of the ac molar magnetic susceptibility (χ'_{ac} and χ''_{ac} , respectively) was obtained from the ac magnetization measured in the temperature range 2 to 55 K, with $H = 0$, and by applying an oscillating magnetic field with a drive amplitude of 0.35 mT at different frequencies in the range 1 to 1000 Hz. The diamagnetic contribution was subtracted from the calculated molar susceptibilities χ .

SUPPLEMENTARY MATERIALS

Supplementary material for this article is available at <http://advances.sciencemag.org/cgi/content/full/3/7/e1700773/DC1>

Supplementary Text

section S1. Synthesis and characterization

section S2. X-ray diffraction

section S3. SEM and EDS analyses

section S4. Kinetic study of $\text{Zn}_{0.59}\text{Co}_{0.41}$ (hfiipbb)

section S5. Neutron powder diffraction

section S6. DFT calculations

section S7. Magnetic susceptibility measurements

table S1. Chemical formula and corresponding molar codes and amount of metal salts used for MOF preparation.

table S2. Results of carbon, hydrogen, and nitrogen analyses and ICP analyses in %weight for all MOFs.

table S3. Crystal and refinement details for $\text{Zn}_{0.89}\text{Co}_{0.11}$ (hfiipbb) (molar code: Zn:Co 1:1) [Cambridge Crystallographic Data Centre (CCDC) number: 1531921].

table S4. Crystal data and structure refinement for $\text{Zn}_{0.89}\text{Co}_{0.11}$ (hfiipbb) at 100 K (molar code: Zn:Co 1:1) (CCDC number: 1531920).

table S5. Crystal and refinement details for $\text{Zn}_{0.59}\text{Co}_{0.41}$ (hfiipbb) (molar code: Zn:Co 1:2) (CCDC number: 1531914).

table S6. Crystal data and structure refinement for $\text{Zn}_{0.59}\text{Co}_{0.41}$ (hfiipbb) at 200 K (molar code: Zn:Co 1:2) (CCDC number: 1531918).

table S7. Crystal data and structure refinement for $\text{Zn}_{0.59}\text{Co}_{0.41}$ (hfiipbb) at 150 K (molar code: Zn:Co 1:2) (CCDC number: 1531919).

table S8. Crystal data and structure refinement for $\text{Zn}_{0.59}\text{Co}_{0.41}$ (hfiipbb) at 100 K (molar code: Zn:Co 1:2) (CCDC number: 1531923).

table S9. Crystal data and structure refinement for $\text{Zn}_{0.59}\text{Co}_{0.41}$ (hfiipbb) at 50 K (molar code: Zn:Co 1:2) (CCDC number: 1531915).

table S10. Crystal data and structure refinement for $\text{Zn}_{0.55}\text{Co}_{0.45}$ (hfiipbb) at room temperature (molar code: Zn:Co 1:4) (CCDC number: 1531916).

table S11. Crystal data and structure refinement for $\text{Zn}_{0.55}\text{Co}_{0.45}$ (hfiipbb) at 100 K (molar code: Zn:Co 1:4) (CCDC number: 1531912).

table S12. Crystal data and structure refinement for $\text{Zn}_{0.21}\text{Co}_{0.79}$ (hfiipbb) at room temperature (molar code: Zn:Co 1:10) (CCDC number: 1531902).

table S13. Crystal data and structure refinement for $\text{Zn}_{0.21}\text{Co}_{0.79}$ (hfiipbb) at 100 K (molar code: Zn:Co 1:10) (CCDC number: 1531903).

table S14. Crystal data and structure refinement for $\text{Zn}_{0.50}\text{Mn}_{0.50}$ (hfiipbb) (molar code: Zn:Mn 1:1) (CCDC number: 1531901).

table S15. Crystal data and structure refinement for $\text{Zn}_{0.96}\text{Ca}_{0.04}$ (hfiipbb) (molar code: Zn:Ca 1:1) (CCDC number: 1531926).

table S16. Crystal data and structure refinement for $\text{Zn}_{0.94}\text{Ca}_{0.06}$ (hfiipbb) (molar code: Zn:Ca 1:2) (CCDC number: 1531924).

table S17. Crystal data and structure refinement for $\text{Zn}_{0.64}\text{Ca}_{0.36}$ (hfiipbb) (molar code: Zn:Ca 1:4) (CCDC number: 1531922).

table S18. Crystal data and structure refinement for $\text{Zn}_{0.48}\text{Ca}_{0.52}$ (hfiipbb) (molar code: Zn:Ca 1:10) (CCDC number: 1531909).

- table S19. Crystal data and structure refinement for $Zn_{0.72}Co_{0.17}Ca_{0.11}(hfpbb)$ (molar code: Zn:Co:Ca 1:1:1) (CCDC number: 1531925).
- table S20. Crystal data and structure refinement for $Zn_{0.33}Co_{0.37}Ca_{0.30}(hfpbb)$ (molar code: Zn:Co:Ca 1:4:4) (CCDC number: 1531907).
- table S21. Crystal data and structure refinement for $Zn_{0.37}Co_{0.14}Ca_{0.49}(hfpbb)$ (molar code: Zn:Co:Ca 1:1:8) (CCDC number: 1531908).
- table S22. Crystal data and structure refinement for $Zn_{0.44}Mn_{0.44}Co_{0.12}(hfpbb)$ (molar code: Zn:Mn:Co 1:1:1) (CCDC number: 1531913).
- table S23. Crystal data and structure refinement for $Zn_{0.54}Mn_{0.37}Co_{0.09}(hfpbb)$ (molar code: Zn:Mn:Co 2:1:1) (CCDC number: 1531910).
- table S24. Crystal data and structure refinement for $Zn_{0.37}Mn_{0.50}Co_{0.13}(hfpbb)$ (molar code: Zn:Mn:Co 1:2:1) (CCDC number: 1531905).
- table S25. Crystal data and structure refinement for $Zn_{0.32}Mn_{0.38}Co_{0.28}(hfpbb)$ (molar code: Zn:Mn:Co 1:1:2) (CCDC number: 1531904).
- table S26. Crystal data and structure refinement for $Zn_{0.22}Mn_{0.32}Co_{0.46}(hfpbb)$ (molar code: Zn:Mn:Co 1:1:8) (CCDC number: 1531900).
- table S27. Crystal data and structure refinement for $Zn_{0.12}Mn_{0.42}Co_{0.46}(hfpbb)$ (molar code: Zn:Mn:Co 1:3:9) (CCDC number: 1531906).
- table S28. Crystal data and structure refinement for $Zn_{0.48}Mn_{0.42}Ca_{0.10}(hfpbb)$ (molar code: Zn:Mn:Ca 1:1:1) (CCDC number: 1531917).
- table S29. Crystal data and structure refinement for $Zn_{0.52}Mn_{0.30}Ca_{0.18}(hfpbb)$ (molar code: Zn:Mn:Ca 1:1:8) (CCDC number: 1531911).
- table S30. Selected bond angles and interatomic lengths of the SBUs involved in the low-temperature magnetism of the MOFs obtained in the Zn:Co system.
- fig. S1. Thermogravimetric-differential thermal analysis (TG-DTA) curve for dried $Zn_{0.89}Co_{0.11}(hfpbb)$ (molar code: Zn:Co 1:1).
- fig. S2. TG-DTA curve for dried $Zn_{0.59}Co_{0.41}(hfpbb)$ (molar code: Zn:Co 1:2).
- fig. S3. TG-DTA curve for dried $Zn_{0.55}Co_{0.45}(hfpbb)$ (molar code: Zn:Co 1:4).
- fig. S4. TG-DTA curve for dried $Zn_{0.21}Co_{0.79}(hfpbb)$ (molar code: Zn:Co 1:10).
- fig. S5. TG-DTA curve for dried $Zn_{0.50}Mn_{0.50}(hfpbb)$ (molar code: Zn:Mn 1:1).
- fig. S6. TG-DTA curve for dried $Zn_{0.96}Ca_{0.04}(hfpbb)$ (molar code: Zn:Ca 1:1).
- fig. S7. TG-DTA curve for dried $Zn_{0.94}Ca_{0.06}(hfpbb)$ (molar code: Zn:Ca 1:2).
- fig. S8. TG-DTA curve for dried $Zn_{0.64}Ca_{0.36}(hfpbb)$ (molar code: Zn:Ca 1:4).
- fig. S9. TG-DTA curve for dried $Zn_{0.52}Ca_{0.48}(hfpbb)$ (molar code: Zn:Ca 1:10).
- fig. S10. TG-DTA curve for dried $Zn_{0.72}Co_{0.17}Ca_{0.11}(hfpbb)$ (molar code: Zn:Co:Ca 1:1:1).
- fig. S11. TG-DTA curve for dried $Zn_{0.33}Co_{0.37}Ca_{0.30}(hfpbb)$ (molar code: Zn:Co:Ca 1:4:4).
- fig. S12. TG-DTA curve for dried $Zn_{0.37}Co_{0.14}Ca_{0.49}(hfpbb)$ (molar code: Zn:Co:Ca 1:1:8).
- fig. S13. TG-DTA curve for dried $Zn_{0.44}Mn_{0.44}Co_{0.12}(hfpbb)$ (molar code: Zn:Mn:Co 1:1:1).
- fig. S14. TG-DTA curve for dried $Zn_{0.54}Mn_{0.37}Co_{0.09}(hfpbb)$ (molar code: Zn:Mn:Co 2:1:1).
- fig. S15. TG-DTA curve for dried $Zn_{0.37}Mn_{0.50}Co_{0.13}(hfpbb)$ (molar code: Zn:Mn:Co 1:2:1).
- fig. S16. TG-DTA curve for dried $Zn_{0.32}Mn_{0.39}Co_{0.28}(hfpbb)$ (molar code: Zn:Mn:Co 1:1:2).
- fig. S17. TG-DTA curve for dried $Zn_{0.22}Mn_{0.32}Co_{0.46}(hfpbb)$ (molar code: Zn:Mn:Co 1:1:8).
- fig. S18. TG-DTA curve for dried $Zn_{0.12}Mn_{0.42}Co_{0.46}(hfpbb)$ (molar code: Zn:Mn:Co 1:3:9).
- fig. S19. TG-DTA curve for dried $Zn_{0.48}Mn_{0.42}Ca_{0.10}(hfpbb)$ (molar code: Zn:Mn:Ca 1:1:1).
- fig. S20. TG-DTA curve for dried $Zn_{0.52}Mn_{0.30}Ca_{0.18}(hfpbb)$ (molar code: Zn:Mn:Ca 1:1:8).
- fig. S21. Normalized powder XRD patterns of $Zn_{0.89}Co_{0.11}(hfpbb)$ (molar code: Zn:Co 1:1): Experimental (black), calculated (blue), and Bragg positions (green).
- fig. S22. Normalized powder XRD patterns of $Zn_{0.59}Co_{0.41}(hfpbb)$ (molar code: Zn:Co 1:2): Experimental (black), calculated (blue), and Bragg positions (green).
- fig. S23. Normalized powder XRD patterns of $Zn_{0.55}Co_{0.45}(hfpbb)$ (molar code: Zn:Co 1:4): Experimental (black), calculated (blue), and Bragg positions (green).
- fig. S24. Normalized powder XRD patterns of $Zn_{0.21}Co_{0.79}(hfpbb)$ (molar code: Zn:Co 1:10): Experimental (black), calculated (blue), and Bragg positions (green).
- fig. S25. Normalized powder XRD patterns of $Zn_{0.50}Mn_{0.50}(hfpbb)$ (molar code: Zn:Mn 1:1): Experimental (black), calculated (blue), and Bragg positions (green).
- fig. S26. Normalized powder XRD patterns of $Zn_{0.96}Ca_{0.04}(hfpbb)$ (molar code: Zn:Ca 1:1): Experimental (black), calculated (blue), and Bragg positions (green).
- fig. S27. Normalized powder XRD patterns of $Zn_{0.94}Ca_{0.06}(hfpbb)$ (molar code: Zn:Ca 1:2): Experimental (black), calculated (blue), and Bragg positions (green).
- fig. S28. Normalized powder XRD patterns of $Zn_{0.64}Ca_{0.36}(hfpbb)$ (molar code: Zn:Ca 1:4): Experimental (black), calculated (blue), and Bragg positions (green).
- fig. S29. Normalized powder XRD patterns of $Zn_{0.52}Ca_{0.48}(hfpbb)$ (molar code: Zn:Ca 1:10): Experimental (black), calculated (blue), and Bragg positions (green).
- fig. S30. Normalized powder XRD patterns of $Zn_{0.72}Co_{0.17}Ca_{0.11}(hfpbb)$ (molar code: Zn:Co:Ca 1:1:1): Experimental (black), calculated (blue), and Bragg positions (green).
- fig. S31. Normalized powder XRD patterns of $Zn_{0.33}Co_{0.37}Ca_{0.30}(hfpbb)$ (molar code: Zn:Co:Ca 1:4:4): Experimental (black), calculated (blue), and Bragg positions (green).
- fig. S32. Normalized powder XRD patterns of $Zn_{0.37}Co_{0.14}Ca_{0.49}(hfpbb)$ (molar code: Zn:Co:Ca 1:1:8): Experimental (black), calculated (blue), and Bragg positions (green).
- fig. S33. Normalized powder XRD patterns of $Zn_{0.44}Mn_{0.44}Co_{0.12}(hfpbb)$ (molar code: Zn:Mn:Co 1:1:1): Experimental (black), calculated (blue), and Bragg positions (green).
- fig. S34. Normalized powder XRD patterns of $Zn_{0.54}Mn_{0.37}Co_{0.09}(hfpbb)$ (molar code: Zn:Mn:Co 2:1:1): Experimental (black), calculated (blue), and Bragg positions (green).
- fig. S35. Normalized powder XRD patterns of $Zn_{0.37}Mn_{0.50}Co_{0.13}(hfpbb)$ (molar code: Zn:Mn:Co 1:2:1): Experimental (black), calculated (blue), and Bragg positions (green).
- fig. S36. Normalized powder XRD patterns of $Zn_{0.32}Mn_{0.39}Co_{0.28}(hfpbb)$ (molar code: Zn:Mn:Co 1:1:2): Experimental (black), calculated (blue), and Bragg positions (green).
- fig. S37. Normalized powder XRD patterns of $Zn_{0.22}Mn_{0.32}Co_{0.46}(hfpbb)$ (molar code: Zn:Mn:Co 1:1:8): Experimental (black), calculated (blue), and Bragg positions (green).
- fig. S38. Normalized powder XRD patterns of $Zn_{0.12}Mn_{0.42}Co_{0.46}(hfpbb)$ (molar code: Zn:Mn:Co 1:3:9): Experimental (black), calculated (blue), and Bragg positions (green).
- fig. S39. Normalized powder XRD patterns of $Zn_{0.48}Mn_{0.42}Ca_{0.10}(hfpbb)$ (molar code: Zn:Mn:Ca 1:1:1): Experimental (black), calculated (blue), and Bragg positions (green).
- fig. S40. Normalized powder XRD patterns of $Zn_{0.52}Mn_{0.30}Ca_{0.18}(hfpbb)$ (molar code: Zn:Mn:Ca 1:1:8): Experimental (black), calculated (blue), and Bragg positions (green).
- fig. S41. SEM image of $Zn_{0.89}Co_{0.11}(hfpbb)$ (molar code: Zn:Co 1:1).
- fig. S42. SEM image of $Zn_{0.59}Co_{0.41}(hfpbb)$ (molar code: Zn:Co 1:2).
- fig. S43. SEM image of $Zn_{0.55}Co_{0.45}(hfpbb)$ (molar code: Zn:Co 1:4).
- fig. S44. SEM image of $Zn_{0.21}Co_{0.79}(hfpbb)$ (molar code: Zn:Co 1:10).
- fig. S45. SEM image of $Zn_{0.96}Ca_{0.04}(hfpbb)$ (molar code: Zn:Ca 1:1).
- fig. S46. SEM image of $Zn_{0.94}Ca_{0.06}(hfpbb)$ (molar code: Zn:Ca 1:2).
- fig. S47. SEM image of $Zn_{0.64}Ca_{0.36}(hfpbb)$ (molar code: Zn:Ca 1:4).
- fig. S48. SEM image of $Zn_{0.48}Ca_{0.52}(hfpbb)$ (molar code: Zn:Ca 1:10).
- fig. S49. SEM image of $Zn_{0.50}Mn_{0.50}(hfpbb)$ (molar code: Zn:Mn 1:1).
- fig. S50. SEM image of $Zn_{0.72}Co_{0.17}Ca_{0.11}(hfpbb)$ (molar code: Zn:Co:Ca 1:1:1).
- fig. S51. SEM image of $Zn_{0.33}Co_{0.37}Ca_{0.30}(hfpbb)$ (molar code: Zn:Co:Ca 1:4:4).
- fig. S52. SEM image of $Zn_{0.37}Co_{0.14}Ca_{0.49}(hfpbb)$ (molar code: Zn:Co:Ca 1:1:8).
- fig. S53. SEM image of $Zn_{0.44}Mn_{0.44}Co_{0.12}(hfpbb)$ (molar code: Zn:Mn:Co 1:1:1).
- fig. S54. SEM image of $Zn_{0.52}Mn_{0.37}Co_{0.09}(hfpbb)$ (molar code: Zn:Mn:Co 2:1:1).
- fig. S55. SEM image of $Zn_{0.37}Mn_{0.50}Co_{0.13}(hfpbb)$ (molar code: Zn:Mn:Co 1:2:1).
- fig. S56. SEM image of $Zn_{0.32}Mn_{0.39}Co_{0.28}(hfpbb)$ (molar code: Zn:Mn:Co 1:1:2).
- fig. S57. SEM image of $Zn_{0.22}Mn_{0.32}Co_{0.46}(hfpbb)$ (molar code: Zn:Mn:Co 1:1:8).
- fig. S58. SEM image of $Zn_{0.12}Mn_{0.42}Co_{0.46}(hfpbb)$ (molar code: Zn:Mn:Co 1:3:9).
- fig. S59. SEM image of $Zn_{0.48}Mn_{0.42}Ca_{0.10}(hfpbb)$ (molar code: Zn:Mn:Ca 1:1:1).
- fig. S60. SEM image of $Zn_{0.52}Mn_{0.30}Ca_{0.18}(hfpbb)$ (molar code: Zn:Mn:Ca 1:1:8).
- fig. S61. SEM image corresponding to $Zn_{0.89}Co_{0.11}(hfpbb)$ crystals (molar code: Zn:Co 1:1).
- fig. S62. SEM image corresponding to $Zn_{0.59}Co_{0.41}(hfpbb)$ crystals (molar code: Zn:Co 1:2).
- fig. S63. SEM image corresponding to $Zn_{0.55}Co_{0.45}(hfpbb)$ crystals (molar code: Zn:Co 1:4).
- fig. S64. SEM image corresponding to $Zn_{0.21}Co_{0.79}(hfpbb)$ crystals (molar code: Zn:Co 1:10).
- fig. S65. SEM image corresponding to $Zn_{0.50}Mn_{0.50}(hfpbb)$ crystals (molar code: Zn:Mn 1:1).
- fig. S66. SEM image corresponding to $Zn_{0.96}Ca_{0.04}(hfpbb)$ crystals (molar code: Zn:Ca 1:1).
- fig. S67. SEM image corresponding to $Zn_{0.94}Ca_{0.06}(hfpbb)$ crystals (molar code: Zn:Ca 1:2).
- fig. S68. SEM image corresponding to $Zn_{0.64}Ca_{0.36}(hfpbb)$ crystals (molar code: Zn:Ca 1:4).
- fig. S69. SEM image corresponding to $Zn_{0.48}Ca_{0.52}(hfpbb)$ crystals (molar code: Zn:Ca 1:10).
- fig. S70. SEM image corresponding to $Zn_{0.72}Co_{0.17}Ca_{0.11}(hfpbb)$ crystals (molar code: Zn:Co:Ca 1:1:1).
- fig. S71. SEM image corresponding to $Zn_{0.33}Co_{0.37}Ca_{0.30}(hfpbb)$ crystals (molar code: Zn:Co:Ca 1:4:4).
- fig. S72. SEM image corresponding to $Zn_{0.37}Co_{0.14}Ca_{0.49}(hfpbb)$ crystals (molar code: Zn:Co:Ca 1:1:8).
- fig. S73. SEM image corresponding to $Zn_{0.44}Mn_{0.44}Co_{0.12}(hfpbb)$ crystals (molar code: Zn:Mn:Co 1:1:1).
- fig. S74. SEM image corresponding to $Zn_{0.54}Mn_{0.37}Co_{0.09}(hfpbb)$ crystals (molar code: Zn:Mn:Co 2:1:1).
- fig. S75. SEM image corresponding to $Zn_{0.37}Mn_{0.50}Co_{0.13}(hfpbb)$ crystals (molar code: Zn:Mn:Co 1:2:1).
- fig. S76. SEM image corresponding to $Zn_{0.32}Mn_{0.39}Co_{0.28}(hfpbb)$ crystals (molar code: Zn:Mn:Co 1:1:2).
- fig. S77. SEM image corresponding to $Zn_{0.22}Mn_{0.32}Co_{0.46}(hfpbb)$ crystals (molar code: Zn:Mn:Co 1:1:8).
- fig. S78. SEM image corresponding to $Zn_{0.12}Mn_{0.42}Co_{0.46}(hfpbb)$ crystals (molar code: Zn:Mn:Co 1:3:9).
- fig. S79. SEM image corresponding to $Zn_{0.48}Mn_{0.42}Ca_{0.10}(hfpbb)$ crystals (molar code: Zn:Mn:Ca 1:1:1).
- fig. S80. SEM image corresponding to $Zn_{0.52}Mn_{0.30}Ca_{0.18}(hfpbb)$ crystals (molar code: Zn:Mn:Ca 1:1:8).
- fig. S81. Normalized Zn and Co atomic ratio versus reaction time in kinetic study of $Zn_{0.59}Co_{0.41}(hfpbb)$ (molar code: Zn:Co 1:2).
- fig. S82. Reaction yield versus reaction time in kinetic study of $Zn_{0.59}Co_{0.41}(hfpbb)$ (molar code: Zn:Co 1:2).
- fig. S83. Variable temperature NPD for $Zn_{0.59}Co_{0.41}(hfpbb)$ (molar code: Zn:Co 1:2).
- fig. S84. Variable temperature NPD for $Zn_{0.21}Co_{0.79}(hfpbb)$ (molar code: Zn:Co 1:10).
- fig. S85. Variable temperature NPD for $Zn_{0.64}Ca_{0.36}(hfpbb)$ (molar code: Zn:Ca 1:4).
- fig. S86. Variable temperature NPD for $Zn_{0.52}Ca_{0.48}(hfpbb)$ (molar code: Zn:Ca 1:10).
- fig. S87. Variable temperature NPD for $Zn_{0.72}Co_{0.17}Ca_{0.11}(hfpbb)$ (molar code: Zn:Co:Ca 1:1:1).
- fig. S88. Variable temperature NPD for $Zn_{0.33}Co_{0.37}Ca_{0.30}(hfpbb)$ (molar code: Zn:Co:Ca 1:4:4).
- fig. S89. Variable temperature NPD for $Zn_{0.37}Co_{0.14}Ca_{0.49}(hfpbb)$ (molar code: Zn:Co:Ca 1:1:8).

fig. S90. Variable temperature NPD for $Zn_{0.54}Mn_{0.37}Co_{0.09}$ (hfpbb) (molar code: Zn:Mn:Co 2:1:1).
 fig. S91. Variable temperature NPD for $Zn_{0.37}Mn_{0.50}Co_{0.13}$ (hfpbb) (molar code: Zn:Mn:Co 1:2:1).
 fig. S92. Variable temperature NPD for $Zn_{0.32}Mn_{0.39}Co_{0.28}$ (hfpbb) (molar code: Zn:Mn:Co 1:1:2).
 fig. S93. Variable temperature NPD for $Zn_{0.48}Mn_{0.42}Ca_{0.10}$ (hfpbb) (molar code: Zn:Mn:Ca 1:1:1).
 fig. S94. ΔE_{form} for the pure and bimetallic structures normalized to the most stable one.
 fig. S95. Partial view of the crystal structure of the helical, rod-shaped inorganic chains built up with alternating tetrahedral and octahedral metal polyhedrons.
 fig. S96. Low-temperature dependence of the product temperature by real component (left y axis) and imaginary component (right y axis) of the ac magnetic susceptibility obtained for the MOF with formula $Zn_{0.59}Co_{0.41}$ (hfpbb).
 fig. S97. Magnetic field dependence of the virgin magnetization curves for $Zn_{0.59}Co_{0.41}$ (hfpbb).
 fig. S98. Low-magnetic field region of hysteresis loops measured at 2 K (circles), 15 K (diamonds), and 30 K (hexagons) for the MOF with formula $Zn_{0.59}Co_{0.41}$ (hfpbb).
 fig. S99. Thermal variation of dc magnetic susceptibility measured in an applied field of 5 mT for the MOF with formula $Zn_{0.59}Co_{0.41}$ (hfpbb).
 fig. S100. Low-temperature dependence of the product temperature by ac magnetic susceptibility (left y axis) and temperature by the imaginary component (right y axis) of the ac magnetic susceptibility obtained for the MOF with formula $Zn_{0.21}Co_{0.79}$ (hfpbb).
 fig. S101. Magnetic field dependence of the virgin magnetization curves for $Zn_{0.21}Co_{0.79}$ (hfpbb).
 fig. S102. Low-magnetic field region of hysteresis loops measured at 2 K (black line), 30 K (red line), and 35 K (blue line) for the MOF with formula $Zn_{0.21}Co_{0.79}$ (hfpbb).
 fig. S103. Thermal variation of magnetic susceptibility for $Zn_{0.21}Co_{0.79}$ (hfpbb).

REFERENCES AND NOTES

- J. B. Goodenough, K.-S. Park, The Li-ion rechargeable battery: A perspective. *J. Am. Chem. Soc.* **135**, 1167–1176 (2013).
- D. E. Farrell, B. S. Chandrasekhar, M. R. DeGuire, M. M. Fang, V. G. Kogan, J. R. Clem, D. K. Finnemore, Superconducting properties of aligned crystalline grains of $Y_1Ba_2Cu_3O_{7-\delta}$. *Phys. Rev. B* **36**, 4025–4027 (1987).
- X. H. Chen, T. Wu, G. Wu, R. H. Liu, H. Chen, D. F. Fang, Superconductivity at 43K in $SmFeAsO_{1-x}F_x$. *Nature* **453**, 761–762 (2008).
- Z. Jin, T. Fukumura, M. Kawasaki, K. Ando, H. Saito, T. Sekiguchi, Y. Z. Yoo, M. Murakami, Y. Matsumoto, T. Hasegawa, H. Koinuma, High throughput fabrication of transition-metal-doped epitaxial ZnO thin films: A series of oxide-diluted magnetic semiconductors and their properties. *Appl. Phys. Lett.* **78**, 3824–3826 (2001).
- C. Yuan, H. B. Wu, Y. Xie, X. W. Lou, Mixed transition-metal oxides: Design, synthesis, and energy-related applications. *Angew. Chem. Int. Ed.* **53**, 1488–1504 (2014).
- T. Fukumura, Z. Jin, M. Kawasaki, T. Shono, T. Hasegawa, S. Koshihara, H. Koinuma, Magnetic properties of Mn-doped ZnO. *Appl. Phys. Lett.* **78**, 958–960 (2001).
- C. de la Cruz, Q. Huang, J. W. Lynn, J. Li, W. Ratcliff II, J. L. Zarestky, H. A. Mook, G. F. Chen, J. L. Luo, N. L. Wang, P. Dai, Magnetic order close to superconductivity in the iron-based layered $LaO_{1-x}F_xFeAs$ systems. *Nature* **453**, 899–902 (2008).
- L. Lin, Y. Yang, L. Men, X. Wang, D. He, Y. Chai, B. Zhao, S. Ghoshroy, Q. Tang, A highly efficient $TiO_2@ZnO$ n-p-n heterojunction nanorod photocatalyst. *Nanoscale* **5**, 588–593 (2013).
- B. Donkova, D. Dimitrov, M. Kostadinov, E. Mitkova, D. Mehandjiev, Catalytic and photocatalytic activity of lightly doped catalysts $M:ZnO$ ($M = Cu, Mn$). *Mater. Chem. Phys.* **123**, 563–568 (2010).
- H. Furukawa, K. E. Cordova, M. O’Keeffe, O. M. Yaghi, The chemistry and applications of metal-organic frameworks. *Science* **341**, 1230444 (2013).
- C. K. Brozek, M. Dincă, Cation exchange at the secondary building units of metal-organic frameworks. *Chem. Soc. Rev.* **43**, 5456–5467 (2014).
- L. M. Aguirre-Díaz, F. Gándara, M. Iglesias, N. Snejko, E. Gutiérrez-Puebla, M. Monge, Tunable catalytic activity of solid solution metal-organic frameworks in one-pot multicomponent reactions. *J. Am. Chem. Soc.* **137**, 6132–6135 (2015).
- Q. Liu, H. Cong, H. Deng, Deciphering the spatial arrangement of metals and correlation to reactivity in multivariate metal-organic frameworks. *J. Am. Chem. Soc.* **138**, 13822–13825 (2016).
- C. Castillo-Blas, N. Snejko, V. A. de la Peña-O’Shea, J. Gallardo, E. Gutiérrez-Puebla, M. A. Monge, F. Gándara, Crystal phase competition by addition of a second metal cation in solid solution metal-organic frameworks. *Dalton Trans.* **45**, 4327–4337 (2016).
- A. Monge, N. Snejko, E. Gutiérrez-Puebla, M. Medina, C. Cascales, C. Ruiz-Valero, M. Iglesias, B. Gómez-Lor, One teflon[®]-like channelled nanoporous polymer with a chiral and new uninodal 4-connected net: Sorption and catalytic properties. *Chem. Commun.* **2005**, 1291–1293 (2005).
- H. C. Zeng, Ostwald ripening: A synthetic approach for hollow nanomaterials. *Curr. Nanosci.* **3**, 177–181 (2007).
- M. O’Keeffe, O. M. Yaghi, Deconstructing the crystal structures of metal-organic frameworks and related materials into their underlying nets. *Chem. Rev.* **112**, 675–702 (2012).
- A. Schoedel, M. Li, D. Li, M. O’Keeffe, O. M. Yaghi, Structures of metal-organic frameworks with rod secondary building units. *Chem. Rev.* **116**, 12466–12535 (2016).
- D. Kim, A. Coskun, Template-directed approach towards the realization of ordered heterogeneity in bimetallic metal-organic frameworks. *Angew. Chem. Int. Ed.* **56**, 5071–5076 (2017).
- B. A. Inc. (Bruker AXS Inc., Madison, Wisconsin, 2015).
- O. V. Dolomanov, L. J. Bourhis, R. J. Gildea, J. A. K. Howard, H. Puschmann, OLEX2: A complete structure solution, refinement and analysis program. *J. Appl. Cryst.* **42**, 339–341 (2009).
- G. M. Sheldrick, A short history of SHELX. *Acta Crystallogr. A* **64**, 112–122 (2008).
- Biovia, Materials Studio 8.0 (2016).
- G. Kresse, J. Furthmüller, Efficiency of ab-initio total energy calculations for metals and semiconductors using a plane-wave basis set. *Comput. Mater. Sci.* **6**, 15–50 (1996).
- G. Kresse, J. Hafner, Ab initio molecular dynamics for liquid metals. *Phys. Rev. B* **47**, 558–561 (1993).
- J. P. Perdew, Y. Wang, Accurate and simple analytic representation of the electron-gas correlation energy. *Phys. Rev. B* **45**, 13244–13249 (1992).
- J. P. Perdew, J. A. Chevary, S. H. Vosko, K. A. Jackson, M. R. Pederson, D. J. Singh, C. Fiolhais, Atoms, molecules, solids, and surfaces: Applications of the generalized gradient approximation for exchange and correlation. *Phys. Rev. B* **46**, 6671–6687 (1992).
- P. E. Blöchl, Projector augmented-wave method. *Phys. Rev. B* **50**, 17953–17979 (1994).
- G. Kresse, D. Joubert, From ultrasoft pseudopotentials to the projector augmented-wave method. *Phys. Rev. B* **59**, 1758–1775 (1999).

Acknowledgments: We acknowledge Institut Laue-Langevin and Spanish Initiatives on Neutron Scattering (SpInS-ILL) for beamtime at instruments D2B and D1B, respectively. We thank E. Rodríguez-Cañas from the Servicio Interdepartamental de Investigación at Universidad Autónoma de Madrid for valuable support with SEM images and EDS analyses acquisition. **Funding:** Work at Instituto de Ciencia de Materiales de Madrid–Consejo Superior de Investigaciones Científicas (CSIC) has been supported by the Spanish Ministry of Economy and Competitiveness (MINECO) Projects MAT2013-45460-R, CTQ2014-61748-EXP, and MAT2016-78465-R. F.G. acknowledges financial support from Fundación General CSIC (Programa ComFuturo) and MINECO (Ramón y Cajal program). Computational time has been provided by the Centre de Supercomputació de Catalunya. This work, developed under the HyMAP project, has received funding from the European Research Council under the European Union’s Horizon 2020 research and innovation program (grant 648319). **Author contributions:** F.G. and Á.M. conceived and coordinated the work. C.C.-B. synthesized and analytically characterized all compounds. C.C.-B., E.G.-P., Á.M., and F.G. collected and analyzed the single-crystal XRD data. C.C.-B. collected the SEM and EDS data. I.P.-O., C.C.-B., and F.G. collected and processed the NPD data. R.S.-P. and J.R.d.P. collected the magnetic susceptibility data and analyzed and interpreted the data. V.A.d.I.P.-O. carried out and analyzed DFT calculations. All authors discussed the data, commented on the discussion, and contributed to the manuscript preparation. **Competing interests:** The authors declare that they have no competing interests. **Data and materials availability:** All data needed to evaluate the conclusions in the paper are present in the paper and/or the Supplementary Materials. Additional data related to this paper may be requested from the authors.

Submitted 6 March 2017
 Accepted 12 June 2017
 Published 21 July 2017
 10.1126/sciadv.1700773

Citation: Castillo-Blas, V. A. de la Peña-O’Shea, I. Puente-Orench, J. R. de Paz, R. Sáez-Puche, E. Gutiérrez-Puebla, F. Gándara, Á. Monge, Addressed realization of multication complex arrangements in metal-organic frameworks. *Sci. Adv.* **3**, e1700773 (2017).

Addressed realization of multication complex arrangements in metal-organic frameworks

Celia Castillo-Blas, Víctor A. de la Peña-O'Shea, Inés Puente-Orench, Julio Romero de Paz, Regino Sáez-Puche, Enrique Gutiérrez-Puebla, Felipe Gándara and Ángeles Monge

Sci Adv 3 (7), e1700773.
DOI: 10.1126/sciadv.1700773

ARTICLE TOOLS

<http://advances.sciencemag.org/content/3/7/e1700773>

SUPPLEMENTARY MATERIALS

<http://advances.sciencemag.org/content/suppl/2017/07/17/3.7.e1700773.DC1>

PERMISSIONS

<http://www.sciencemag.org/help/reprints-and-permissions>

Use of this article is subject to the [Terms of Service](#)

Science Advances (ISSN 2375-2548) is published by the American Association for the Advancement of Science, 1200 New York Avenue NW, Washington, DC 20005. 2017 © The Authors, some rights reserved; exclusive licensee American Association for the Advancement of Science. No claim to original U.S. Government Works. The title *Science Advances* is a registered trademark of AAAS.